Next Materials 12 (2026) 102419

Contents lists available at ScienceDirect

Next Materials

journal homepage: www.sciencedirect.com/journal/next-materials

Research article

Influence of 3D architecture on photocatalytic efficiency in structures derived from a novel boron acrylate via UV-SLA and pyrolysis

Greta Merkininkaitė [a,*], Robertas Virkėtis [b], Simas Šakirzanovas [a,b]

[a] Center for Physical Sciences and Technology, Saulėtekis av. 3, Vilnius, LT-10257, Lithuania
[b] Institute of Chemistry, Faculty of Chemistry and Geosciences, Vilnius University, Naugardukas 24, Vilnius, LT-03225, Lithuania

ARTICLE INFO

Keywords:
Boron acrylate
3D architecture
UV stereolithography
Pyrolysis
Boron-based ceramic
Photocatalyst
Water purification

ABSTRACT

Additive manufacturing enables the fabrication of photocatalytic three-dimensional architectures with precisely controlled geometry, offering new opportunities to optimize light and material interaction, structural stability, and catalyst reusability for water-treatment applications. In this work, monolithic 3D photocatalysts were fabricated by UV stereolithography using a newly synthesized boron and nitrogen-containing acrylate photoresin, followed by high-temperature pyrolysis to obtain polymer-derived ceramic structures. The chemical structure of the photoresin was confirmed by ^{1}H NMR spectroscopy, while refractive index measurements demonstrated its suitability for stereolithography. Thermal analysis revealed a multistep polymer-to-ceramic conversion with significant mass loss and densification, accompanied by pronounced geometry-dependent volumetric shrinkage during pyrolysis. Phase transformation monitored by X-ray diffraction showed a transition to the hexagonal boron nitride phase after high-temperature treatment. A range of architected geometries, including channel, lattice, and gyroid-based cubic and rounded models, were evaluated to assess the influence of 3D architecture on photocatalytic behavior. Photocatalytic activity was investigated via Rhodamine B degradation under halogen lamp irradiation. Structures annealed at 500 °C and 900 °C exhibited limited activity, whereas samples treated at 1200 °C showed a marked increase in performance despite reduced surface area caused by shrinkage. When normalized to photocatalyst surface area, curved gyroid-type architectures outperformed channel and lattice designs, reaching a maximum specific degradation efficiency of 355.01 mg/m^2. These results demonstrate that the photocatalytic response is governed by the combined effects of the composition of the material and three-dimensional architectural model.

1. Introduction

Photocatalysis is increasingly pursued as a sustainable, solar-driven route for water treatment, particularly for the degradation of organic pollutants [1]. Despite major advances in semiconductor materials, practical deployment is still constrained by catalyst configuration. Photocatalytic stochastic fiber catalysts exhibit a high specific surface area, however, their disordered morphology results in limited light accessibility and low resistance to high mechanical pressure. While dispersed nanoparticle photocatalysts often aggregate, suffer from light attenuation within turbid suspensions, and require cost-intensive separation after treatment, which collectively reduces process efficiency and limits scalability [2].

Monolithic 3D photocatalysts address these limitations [3]. In contrast to nanoparticle slurries and stochastic fibers, 3D monoliths enable stable reuse, minimize catalyst loss and secondary contamination, and are readily implemented in continuous-flow operation because of their mechanically robust and retrievable architecture [4]. Importantly, in additive manufacturing, geometry becomes a tunable parameter, enabling performance gains through architecture rather than relying solely on chemical modification [5].

The photocatalytic efficiency of a monolith is mostly governed by the nature of the material and 3D shape, which simultaneously controls liquid flow and interaction of light and material [6]. Architecture determines light permeability and solution flow distribution, thereby regulating material residence time, boundary-layer thickness, and the renewal of reactants at active surfaces [7]. 3D photocatalyst pore size, connectivity, and accessible surface area dictate diffusion pathways and product removal. At the same time, geometry governs how light interacts with the catalyst: internal architectural features can function as photon-management elements, trapping and redistributing irradiation to increase the effective optical path length and reduce losses from reflection or shading [8]. The combination of architecture with

* Corresponding author.
E-mail address: greta.merkininkaite@chgf.vu.lt (G. Merkininkaitė).

https://doi.org/10.1016/j.nxmate.2026.102419
Received 9 March 2026; Received in revised form 26 May 2026; Accepted 1 June 2026
Available online 12 June 2026

functional material can further boost efficiency, for example, by incorporating heterojunctions to suppress electron–hole recombination [9]. Together, these considerations position the 3D structural architecture as a powerful strategy to improve photocatalytic reactors and accelerate translation to scalable water-treatment technologies.

In this study, the primary objective was to evaluate the influence of 3D shape and architecture on photocatalytic efficiency using monolithic ceramic photocatalysts fabricated by combining the synthesis of new material, additive manufacturing, and pyrolysis. UV stereolithography was employed to produce complex 3D structures from a boron and nitrogen-containing photoresin, followed by high-temperature pyrolysis to obtain mechanically stable boron nitride-based ceramic photocatalysts. A series of distinct architectures, including honeycomb, lattice, and gyroid-based cubic and rounded geometries, were designed to provide controlled variations in surface-to-volume ratio, material flow, and light-interaction characteristics [10,11]. This work demonstrates how the 3D shape architecture of a photocatalyst can influence photocatalytic degradation performance. The results provide valuable guidelines for developing efficient (achieved specific degradation efficiency 355.01 mg/m^2), reusable, and scalable monolithic photocatalysts for environmental applications.

2. Experimental

The following section describes the experimental procedures, which consisted of several stages. The 4,4'-(2,2'-bis (ethane-2,1-diyl) bis(azanediyl)bis(ethane-2,1-diyl) bis(oxy)) bis(10-methyl-9-oxo-3,5,8-trioxa-4-boraun- dec-10-ene-4,1-diyl)bis(2-methylacrylate) (DEABMA) monomer was synthesized via esterification, and its formation and yield were confirmed by ^{1}H NMR spectroscopy. Refractive index (RI) measurements, Fourier transform infrared (FTIR) spectroscopy, and thermal analysis were performed on both the monomer and polymer samples to evaluate chemical transformations during the process. Finally, 3D boron-based photocatalysts (PhCs) were fabricated by combining UV stereolithography with high-temperature treatment. The morphology and structural evolution were examined by X-ray diffraction (XRD). Photocatalytic activity was assessed through dye degradation experiments.

2.1. Materials and synthesis

The DEABMA monomer was synthesized through an esterification reaction. The synthesis route was based on the procedure reported for 4,4'-(2,2'-oxybis(ethane-2,1-diyl)bis (oxy))bis(10-methyl-9-oxo-3,5,8-trioxa-4-boraundec-10-ene-4,1-diyl)bis(2-methylacrylate) (BoMAF) synthesis [12], with diethylene glycol replaced by diethanolamine in order to introduce a nitrogen atom into the chemical structure. To the best of our knowledge, neither of these acrylates (DEABMA or BoMAF) has been employed in 3D photopolymerization.

The synthesis of DEABMA monomer is summarized as follows: 25.0 ml of toluene (HPLC, Lab-Scan), 79 µl of hydrophosphorus acid solution (H_3PO_2, 50%, Acros Organics) as a catalyst, 6.24 ml (0.0647 mol) of diethanolamine (DEA, an.gr., Eurochemicals), 5.00 g (0.0809 mol) of boric acid ($B(OH)_3$, 99.5%, Sigma Aldrich), 0.078 g (0.0006 mol) of 4-methoxyphenol inhibitor (MeHQ, 99%, Acros Organics) and 13.77 ml (0.1132 mol) of 2-hydroxyethyl methacrylate (HEMA, 97%, Sigma Aldrich) were added to a 100 ml three-neck round-bottom flask equipped with a magnetic stirrer, a Dean–Stark adapter, and a condenser. The reaction mixture was stirred and heated to 70 °C until complete dissolution of all components. After dissolution, the reaction temperature was raised to the reflux temperature 125 °C, and the water (4.36 ml) was removed by azeotrope distillation with the Dean–Stark apparatus. End of the reaction was determined by monitoring the amount of water removed. Toluene was removed by vacuum distillation. The product, presented in Fig. 1(a) (DEABMA monomer), was a transparent, colorless, and viscous liquid. Finally, diphenyl-(2,4,6-trimethylbenzoyl) phosphine oxide (TPO, 97%, Sigma Aldrich) was added as a photoinitiator at 2 wt% of the total mass of the product mixture. After complete dissolution of the initiator, the obtained clear photosensitive resin was further used for stereolithography.

2.2. Characterization

The ^{1}H NMR spectrum of the synthesized DEABMA was recorded in hexadeuterodimethyl sulfoxide (DMSO-d_6, 99.9%, Sigma-Aldrich) at 22 °C using a Bruker Ascend 400 MHz spectrometer. Chemical shifts were referenced to the residual solvent signal at 2.50 ppm (δ, DMSO-d_6).

Dynamic viscosity measurements of the synthesized DEABMA was carried out using an Anton Paar DV-2P L digital rotational viscometer at 22 °C and 40 °C. The desired temperature was maintained by thermostating the monomer samples. The operating principle of this viscometer is based on monitoring the resistance of the sample to the rotation of the probe.

The refractive indices (RI) of DEABMA were measured using an Abbemat WR MW refractometer equipped with a YAG (yttrium aluminium garnet) prism and an LED light source operating at wavelengths of 436.5, 486, 513.5, 546.3, 589.3, and 643.3 nm. All measurements were performed at a constant temperature of 25 °C.

FTIR spectra were recorded using a Bruker ALPHA FTIR spectrometer equipped with a room-temperature DLATGS detector. Each spectrum was acquired from 100 interferogram scans at a resolution of 2 cm^{-1} over the spectral range of 4000–485 cm^{-1}.

Thermogravimetric analysis (TGA), differential scanning calorimetry (DSC), and derivative thermogravimetry (DTG) were performed using a PerkinElmer Pyris 1 instrument. Polymeric DEABMA samples were analyzed under a nitrogen atmosphere from 30 °C to 900 °C at a heating rate of 5 °C/min.

X-ray diffraction (XRD) data for the annealed samples were collected using a Rigaku Miniflex II diffractometer operating in Bragg–Brentano ($\theta/2\theta$) geometry with Cu Kα radiation. The instrument parameters were as follows: a step size of 0.01°, a scan rate of 5 °/min, and a 2θ range of 5°–80°.

Scanning electron microscopy (SEM) images of the surface morphology of the fabricated 3D structures were acquired using a SEM Hitachi FlexSEM 1000 II instrument.

UV–Vis absorption spectra were recorded using a Perkin Elmer Lambda 35 spectrometer over the wavelength range of 350–700 nm, with a step size of 1 nm and a scan speed of 8 nm/s.

2.3. 3D photopolymerization and post-processing

3D models were created using Blender software and are shown in Fig. 2. The selected models include commonly used geometries: a honeycomb structure (A), a diamond-type lattice (B), gyroid structures with solid walls (C and D) or mesh-like walls (F), a cage-like lattice (E), and spherical gyroids with solid (G) or mesh-like walls (H). For all 3D models, the dimensions along the x, y, and z axes were set to 20 mm.

Polymeric 3D structures were printed using an Original Prusa SL1S SPEED stereolithography system equipped with an FPS1 Mini Heater to maintain the resin temperature at 40 °C, thereby reducing resin viscosity and ensuring sufficient flow during fabrication. The printing parameters were as follows: a layer thickness of 25 µm, a layer exposure time of 15 s, and a UV LED screen with an emission maximum at 405 nm as the light source. After printing, the structures were washed in ethanol for 30 min, post-cured for 2 h using an Anycubic Wash and Cure Machine 2.0 (405 nm emission), and subsequently thermally cured at 110 °C for an additional 2 h.

To convert the polymer structures into crystalline phases and remove organic components, the samples underwent a two-step thermal treatment. In the first step, the structures were annealed on corundum

substrates at temperatures up to 500 °C for 1 h under vacuum, with a heating rate of 1 °C/min. Vacuum conditions and slow heating were essential to minimize structural deformation. In the second step, the structures were further heated under a nitrogen atmosphere at 900 °C, 1200 °C, and 1500 °C for 1 h, using a ramp rate of 5 °C/min.

2.4. Photocatalytic activity evaluation

The photocatalytic activity of the 3D samples annealed at 500 °C under vacuum and at 900 °C, 1200 °C, and 1500 °C in a nitrogen atmosphere, was evaluated by monitoring the degradation of Rhodamine B ($C_{28}H_{31}ClN_2O_3$, 95%, Sigma Aldrich) in an aqueous solution under a low voltage halogen reflector lamp (Radium) irradiation. The lamp operated at 12 V with a nominal current of 4.17 A. Its rated luminous flux was 510 lm, with a luminous intensity of 2600 cd, a beam angle of 24°, an efficacy of 10.2 lm/W, and a color temperature of 3000 K. The emission spectrum of the halogen lamp is comparable to solar radiation in the visible and near-infrared regions, although it contains a lower fraction of UV radiation relative to the solar spectrum [13]. The lamp irradiation spectrum is available on the official manufacturer's website [14].

A stock solution of Rhodamine B was prepared by dissolving 10 mg of dye in 1 L of distilled water (10 mg/L). For each Rhodamine B degradation test, 20 mL of the solution was transferred into a 50 mL glass beaker. Individual 3D PhC samples were placed in the beakers and stirred at 1200 rpm with a magnetic stirrer. A control experiment was conducted under identical conditions without the PhC sample.

The initial absorbance of the solution was measured before irradiation. The samples were then exposed to halogen lamp light, and the absorbance of Rhodamine B solutions was recorded at intervals of 15, 30, 45, 60, 90, and 120 min during irradiation.

3. Results and discussion

3.1. Characterization of the initial material

The chemical composition and purity of the synthesized DEABMA monomer were evaluated by ^{1}H NMR spectroscopy. The synthesis procedure of the DEABMA monomer is described in Section 2.1, and the chemical structure of the DEABMA monomer is shown in Fig. 1(a). To confirm the successful synthesis of DEABMA, ^{1}H NMR spectrum was recorded in DMSO-d_6 (δ = 2.50 ppm) (Fig. 1(b)).

The peaks at 6.06 (*a*), 6.02 (*s*), 5.89 (*r*), 5.69 (*t*), 5.68 (*b*), 5.49 (*q*) ppm are attributed to vinyl =CH_2 protons of the methacrylate moiety. Signals at 4.35 (*w*), 4.24 (*o*), 4.09 (*d*) and 3.64 (*n*), 3.60 (*e*), 3.48 (*x*) ppm correspond to oxymethylene -CH_2- protons neighboring ester and ether oxygen atoms of the HEMA fragment, respectively. Resonances at 3.37 (*m*), 3.26 (*j*), 3.20 (*f*) and 3.03 (*i*) ppm are assigned to oxymethylene -CH_2- protons adjacent to ether oxygen atoms in the DEA fragment. The resonances at 2.88 (*g*), 2.69 (*l*), 2.67 (*k*) and 2.64 (*h*) ppm are attributed to -CH_2- protons neighboring the amino group of the DEA moiety. Three peaks at 1.88 (c), 1.86 (*u*) and 1.82 (*p*) ppm corresponds to the methyl protons characteristic of the methacrylate group.

Additional signals in the spectrum indicate that the resin contains side products and unreacted reagents. The resonances at 5.10 and 4.94 ppm correspond to vinyl =CH_2 protons of the HEMA. A broad peak at 4.80 ppm is assigned to amine protons characteristic of DEA fragments. Resonances in the range of 4.25–3.04 ppm are attributed to oxymethylene -CH_2- protons adjacent to ester and ether oxygen atoms of the HEMA moieties and to ether oxygen atoms in the DEA fragments. The peaks observed between 3.01 and 2.30 ppm are assigned to -CH_2- protons neighboring the amine group characteristic of DEA moieties, while the signal at 1.84 ppm is attributed to methyl protons of the HEMA.

The degree of HEMA esterification was determined from the ^{1}H NMR data by comparing the integrals of the signals of HEMA (δ = 5.10 ppm) and DEABMA (δ = 6.06, 6.02 and 5.89 ppm). The sum of the integrals corresponding to DEABMA was divided by the sum of all four integrals and multiplied by 100%. The calculated degree of HEMA esterification was 76%. Despite the product not being chemically pure, it is well-suited for 3D stereolithography, and the existing impurities do not hinder photopolymerization; therefore, it is referred to hereafter as DEABMA.

FTIR spectroscopy was employed to identify the functional groups present in the DEABMA monomer and to monitor changes in the vinyl groups upon polymerization. Fig. 1(c) presents the FTIR spectra of the DEABMA monomer (green curve) and its polymerized (orange curve) form. Following UV photopolymerization and post-curing at 110 °C for 2 h, the obtained 3D polymeric structures exhibited yellowish coloration and showed no visible cracks or structural defects, as depicted in Fig. 2.

The FTIR spectra of the monomer and polymer display similar band positions for the main functional groups, confirming the preservation of the borate ester backbone after polymerization. A broad absorption band centered at approximately 3300 cm^{-1} is assigned to O–H stretching vibrations, originating from residual hydroxyl groups, while a weak band at 3660 cm^{-1} is attributed to BO–H stretching vibrations. The presence of this peak and the functional group confirms an incomplete esterification reaction during synthesis. However, after polymerization and subsequent heating at 110 °C, this peak disappears, confirming complete post-esterification. Two absorptions peaks at 2965 cm^{-1} and 2840 cm^{-1} region correspond to asymmetric and symmetric stretching vibrations of aliphatic CH_2 groups.

A strong absorption band at 1720 cm^{-1} is assigned to the C=O stretching vibration of the ester groups, while the peak at 1640 cm^{-1} corresponds to the vinyl group C=C stretching vibration in the monomer, which is responsible for the compound participation in subsequent photopolymerization. Upon polymerization, the intensity of the C=C stretching peak is significantly reduced, indicating the consumption of vinyl groups and confirming successful photopolymerization of the DEABMA monomer. The peak observed at 1600 cm^{-1} is attributed to N–H bending vibrations, confirming the incorporation of diethanolamine into the molecular structure. Additionally, the peak at 1390 cm^{-1} is assigned to C–N stretching vibrations, further confirming the presence of amine functionalities in both the monomer and the polymer. Most characteristic absorption peaks remain unchanged, indicating that polymerization proceeds via the acrylate double bonds without altering the borate ester framework.

The optical properties of the synthesized DEABMA were investigated by measuring the refractive indices of both the monomer and the corresponding polymer. Fig. 1(d) shows the wavelength-dependent refractive index values at 25 °C across the visible spectral region. Refractive index measurements provide valuable information about light–matter interactions in photoresins and can also reflect changes in material density associated with polymer formation [15].

For both the DEABMA monomer and polymer, the refractive index varies linearly with increasing wavelength over the investigated range from 436.5 to 643.3 nm, which is characteristic of normal optical dispersion. The monomer displays refractive index values decreasing from about 1.500 to 1.484, whereas the polymerized material shows systematically higher values, ranging from approximately 1.525 to 1.513. The observed increase in refractive index upon polymerization is indicative of molecular packing and densification arising from the formation of a crosslinked polymer. This change in optical density was expected because monomer units are converted into a more rigid macromolecular structure. In the context of UV stereolithography, such refractive index differences are important, as they influence light propagation, curing depth, and voxel size during fabrication. Accurate refractive index characterization is therefore essential for controlling feature resolution and ensuring reproducible printing performance [16].

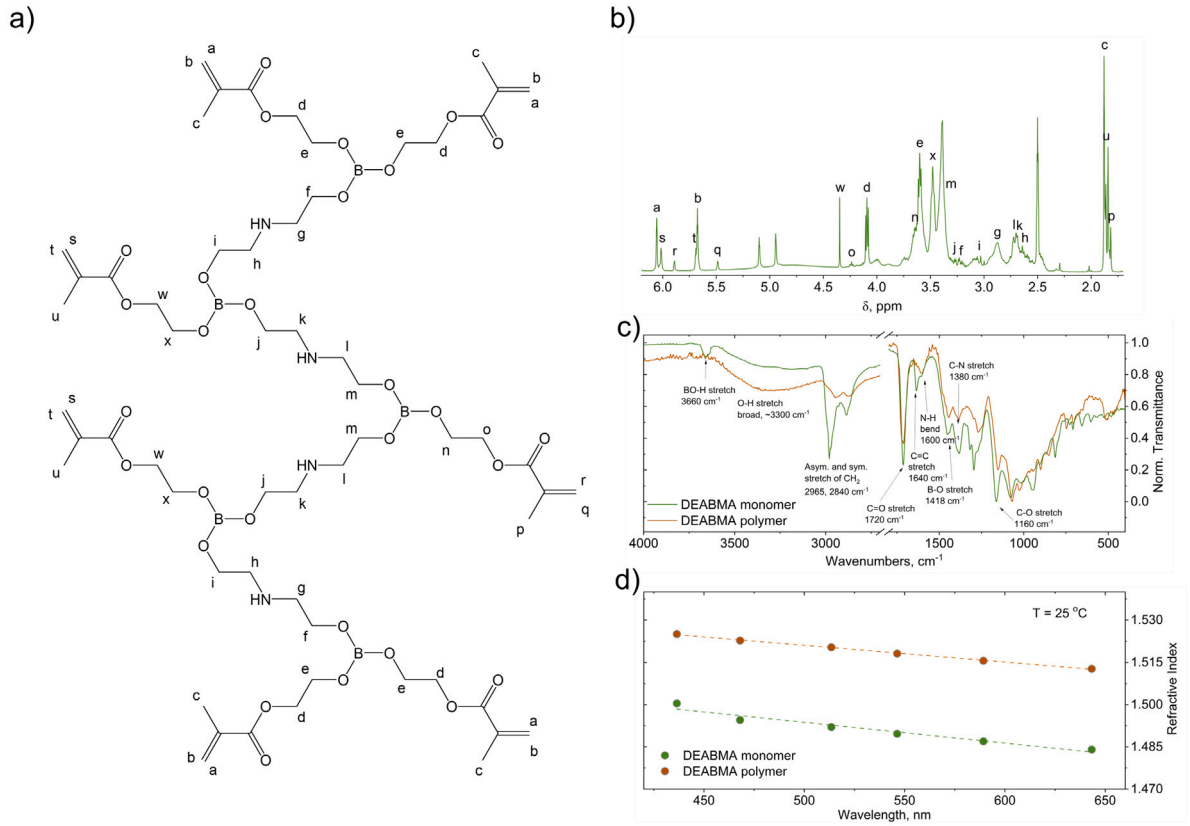

Fig. 1. Chemical composition analysis of the synthesized material: (a) chemical structure of the DEABMA monomer, (b) H^1 NMR spectrum of the synthesized starting material, (c) FTIR spectra of the DEABMA before and after photopolymerization, (d) refractive indices (RI) of the DEABMA and its polymer.

The measured refractive index values for DEABMA fall within the range reported for acrylate-based photoresins (1.4445–1.5454) and their polymers (1.4804–1.5632), measured at 656 nm wavelength [17], supporting the suitability of this material for stereolithographic 3D printing applications not only under UV irradiation but also within the visible spectral range.

3.2. Fabrication and properties evaluation of 3D inorganic structures

To evaluate the influence of 3D architecture on photocatalytic performance in water treatment applications, eight distinct geometries were designed and fabricated [10]. The efficiency of a 3D photocatalyst is strongly governed by its accessible surface area, light penetration and scattering within the structure, and the flow of the liquid through the photocatalyst during photocatalysis [5,9,11]. Unlike conventional powder photocatalysts, architected 3D structures allow these parameters to be varied through geometric shape. Therefore, architectural optimization is a critical factor in photocatalytic efficiency. The selected 3D architectures (see Fig. 2) represent a diverse set of commonly used and functionally relevant geometries, including a honeycomb structure (A), a diamond-type lattice (B), gyroid architectures with solid walls (C and D) or mesh-like walls (F), a cage-like lattice (E), and spherical gyroid structures with either solid (G) or mesh-like walls (H). These models highlight the intended architectural features, including wall thickness, connectivity, pores, overall symmetry, different surface to volume ratios, and light–matter interaction pathways. Channel and lattice geometries (A and E) promote directional fluid flow and reduce liquid transport limitations. In contrast, more complex structures, such as gyroids (C, D, and F) or curved (G and H), and interconnected structures enhance light and material interaction areas.

The top row of Fig. 2 presents the eight designed 3D geometries for fabrication. The second row shows the corresponding polymeric scaffolds fabricated by UV stereolithography using the DEABMA photoresin, demonstrating successful shape reproduction. Upon UV exposure, the TPO photoinitiator absorbs photons and undergoes homolytic cleavage of its weakest bond, generating highly reactive radical species. These radicals add to the vinyl groups of DEABMA monomers, forming active chain-propagating radical centers. Polymerization proceeds via successive radical additions to monomer double bonds, resulting in stepwise growth of the polymer backbone. Chain termination occurs through radical–radical coupling and disproportionation reactions, ultimately producing a crosslinked polymer network [18]. 3D printing was carried out with the resin maintained at 40 °C, reducing its viscosity from 446480 mPa s (at 22 °C) to 24194 mPa s, similar to the viscosity of chocolate syrup [19] and ensuring sufficient flow during fabrication.

The third row provides close-up optical microscopy images, revealing the local surface morphology and internal features of the structures printed after post-curing at 110 °C. The lower rows display the same structures after high-temperature pyrolysis (500 °C under vacuum, 900 °C, 1200 °C and 1500 °C under N_2), resulting in inorganic photocatalysts that exhibit significant volumetric shrinkage while largely preserving their original architectural shape. This shrinkage-induced densification is a key advantage of the polymer-derived ceramic approach, enabling the fabrication of mechanically stable, self-assisted monolithic photocatalysts. Most geometries (A, C, D, E, G, H in the whole temperature range) maintain their overall shape and connectivity after pyrolysis, indicating thermal and structural stability. An exception is structure B, which lost its porosity already after printing and underwent significant deformation during subsequent heating. In addition, the mesh-type structures (F and G) did not exhibit internal cavities within their walls after printing and instead showed only a rough surface relief. However, these structures retained their overall geometry after heating. This behavior confirms that the synthesized DEABMA is not suitable for printing sharp or highly intricate geometries. In addition, structure H appeared partially fused after annealing

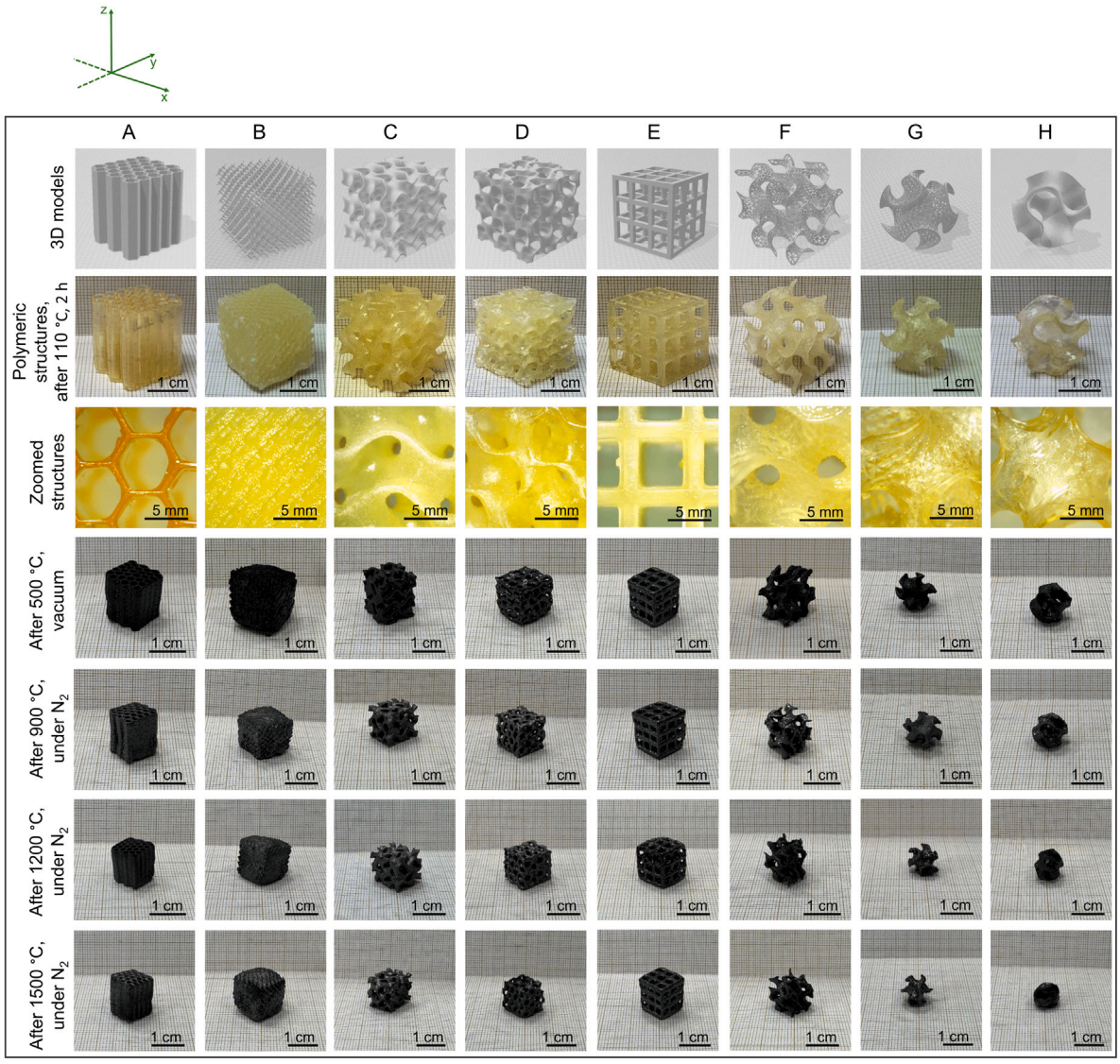

Fig. 2. Overview of architected 3D structures fabricated by UV stereolithography and subsequently converted into inorganic materials by high-temperature pyrolysis. The top row shows the geometries designed in Blender, the second and third rows present the as-printed and pre-heated at 110 °C DEABMA polymeric scaffolds together with optical-microscope close-up images, while the lower rows display the corresponding shrunken structures after pyrolysis (500 °C under vacuum, 900 °C, 1200 °C and 1500 °C under N_2). The comparison illustrates how different lattice topologies preserve their overall architecture through fabrication and densification despite significant volumetric shrinkage and morphological changes—except for structure B, which exhibits pronounced deformation already after annealing at 500 °C in vacuum. Additionally, the wall features of structures F and G after printing did not reproduce the mesh-like surfaces present in the 3D models and instead were printed as solid walls.

at the highest temperature of 1500 °C. In contrast, structure G retained its overall geometry even after annealing at maximum temperature, indicating that mesh-type walls help reduce structural deformation during shrinkage.

SEM analysis of two structures, E and H, was additionally performed to confirm the changes in surface morphology (see Fig. 3). The results reveal a clear temperature-dependent evolution in both structures. Up to 1200 °C, the surfaces remain relatively rough, with visible defects and increasing heterogeneity. At 1200 °C, a marked increase in porosity is observed, indicating intensified decomposition and material restructuring. Further heating to 1500 °C leads to partial melting and sintering, which smoothens the surface and reduces the apparent porosity due to pore coalescence and closure.

During high-temperature treatment of metal–organic 3D structures, not only do their chemical structure and associated optical, physical, and mechanical properties change, but the structures also undergo densification and significant shrinkage. Therefore, the estimated surface areas of the annealed structures before and after heat treatment were evaluated. The estimated surface areas were calculated using Blender software while accounting for shrinkage along the x, y, and z axes, and the results are presented in Fig. 4(a).

It was observed that for some 3D-printed polymeric structures, particularly those containing a large amount of printed material along the *z*-axis, the estimated surface areas were slightly larger than those of the corresponding digital 3D models. For example, in the case of structure A, the surface area of the 3D model was 8805 mm^2, while the surface area of the printed polymeric structure reached 8853 mm^2. This effect can be attributed to the material's higher refractive index. Due to light refraction and scattering within the material, as well as light penetration beyond the intended exposure region, the effective polymerized volume can become larger than defined in the digital model. This effect is particularly pronounced in vertically dense or thick structures, leading to subtle geometric deviations and an increase in surface area.

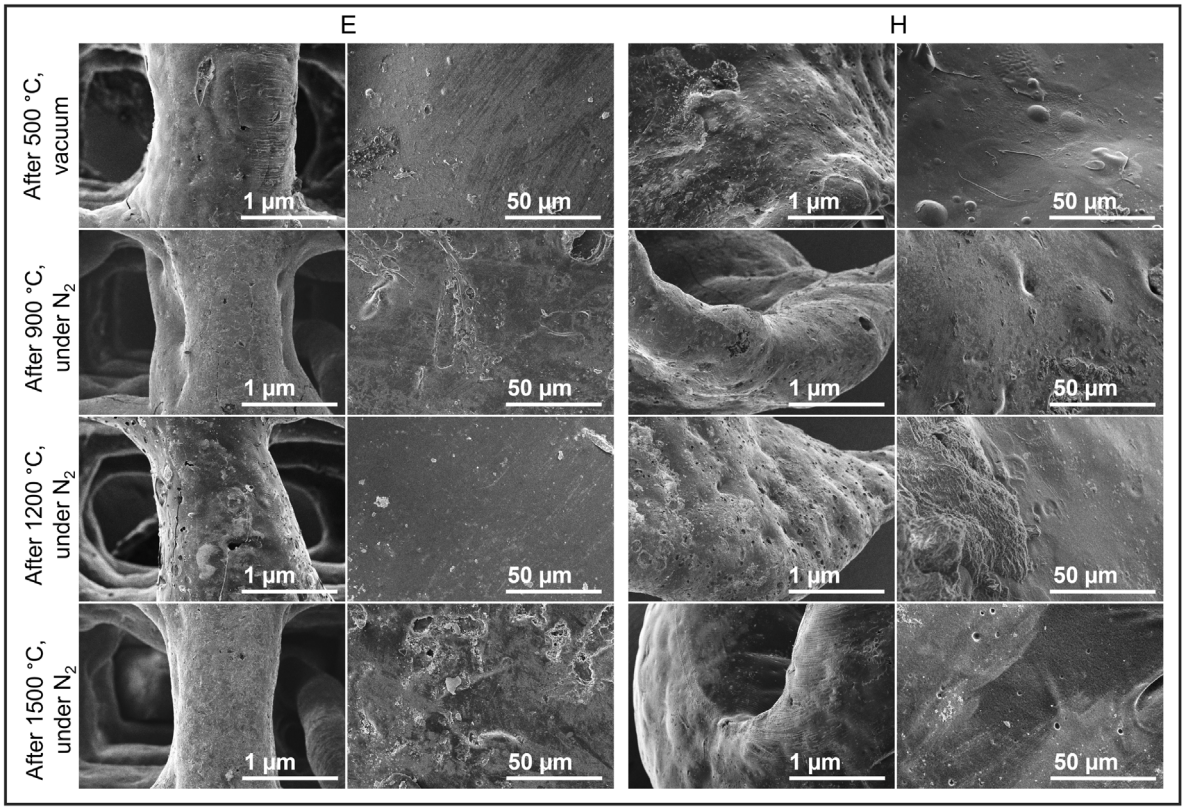

Fig. 3. SEM images of E and H-type 3D structures after thermal treatment at 500 °C in vacuum and at 900 °C, 1200 °C, and 1500 °C in a nitrogen atmosphere, shown at different magnifications (scale bars: 1 μm and 50 μm). Up to 1200 °C, both structures exhibit pronounced surface irregularities and defects. At 1200 °C, a significant increase in porosity is observed, with numerous pores forming on the surface. After treatment at 1500 °C, the structures and their surface pores undergo partial melting/sintering, resulting in smoother surfaces and partial pore closure.

Among the investigated polymeric samples, the largest surface area was measured for structure A (8853 mm^2), while the smallest surface area was observed for structure H (1617 mm^2). All structures exhibited a high degree of shrinkage during thermal treatment. After annealing at 1500 °C, the estimated surface area of structure A decreased to 3525 mm^2 (surface area shrinkage of 60.2%), whereas structure H exhibited a surface area of only 351.4 mm^2 (surface area shrinkage of 78.3%) at the highest annealing temperature.

Accurate determination of surface areas is essential for the evaluation of the photocatalytic performance of the fabricated structures, as photocatalytic activity is directly related to the available active surface area to reactants. Expressing photocatalytic efficiency per unit surface area enables a direct comparison of different architectures by emphasizing differences in light–structure interaction and fluid permeation arising from the 3D geometry [7,20], while eliminating the influence of variations in total surface area.

To evaluate the thermal behavior and mass evolution of the polymerized material upon heating, thermogravimetric analysis (TGA) coupled with derivative thermogravimetry (DTG) and differential scanning calorimetry (DSC) was performed. The polymerized sample (without post-curing at 110 °C) was heated from room temperature to 900 °C under a nitrogen atmosphere. The resulting TGA, DTG, and DSC curves as a function of temperature are shown in Fig. 4(b).

The thermal degradation of the polymer proceeds through several stages, as evidenced by multiple peaks in DTG and DSC curves. At low temperatures (up to ≈100 °C), only minor mass changes are observed, indicating good thermal stability of the polymeric network and the absence of significant volatile loss. As the temperature increases, the first noticeable mass-loss region appears at 200 °C temperature, characterized by a DTG minimum with a maximum weight-loss rate of approximately −1.69%/min. This stage is attributed to the evaporation of residual low-molecular-weight compounds, such as unreacted HEMA, and the initial cleavage of thermally unstable bonds within the polymer matrix (weight loss up to 31.19%). Further heating leads to a more pronounced degradation step, marked by a dominant DTG minimum with a maximum weight-loss rate of −4.90%/min at 330 °C temperature. This region corresponds to the main decomposition of the organic polymer backbone, including the breakdown of C=O, C–O and C–C bonds [21], resulting in a weight loss of 33.16%. A subsequent degradation event is observed at higher temperatures, with a DTG minimum of −3.49%/min, indicating continued decomposition of remaining organic fragments and further densification of the material.

Concurrently, the DSC curve reveals an endothermic process at elevated temperatures, associated with structural rearrangements and the gradual formation of an inorganic structure. In this temperature range, the mass loss slows significantly and approaches stabilization, suggesting the completion of organic decomposition and the onset of inorganic phase formation. At the highest temperatures, only minor additional mass changes are detected, and the final remaining material weight is 13.69%. Overall, the combined TGA, DTG, and DSC results demonstrate a multistep thermal transformation process involving initial evaporation, polymer decomposition, and final conversion into an inorganic phase. These results provide insight into the thermal treatment conditions required for controlled polymer to inorganic conversion.

To assess changes in chemical bonding after thermal treatment, FTIR spectroscopy was performed on DEABMA-derived structures annealed at 500 °C under vacuum followed by heat treatments at 900 °C, 1200 °C, and 1500 °C under a nitrogen atmosphere (Fig. 4c).

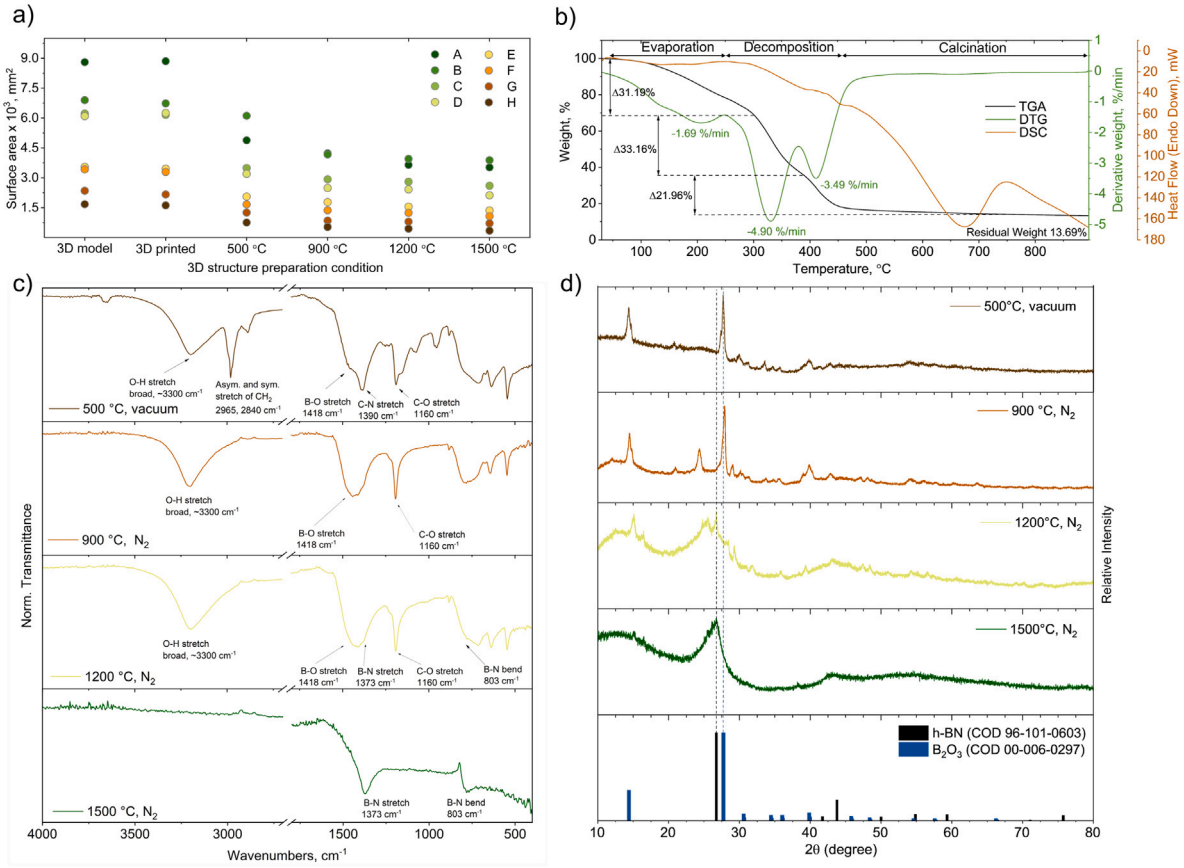

Fig. 4. Properties evaluation of inorganic structures. (a) Surface areas of the 3D models and the estimated surface areas of the polymeric and annealed structures at the corresponding temperatures (500–1500 °C), illustrating a progressive decrease in surface area with increasing annealing temperature. The estimated surface areas were calculated using Blender software while accounting for shrinkage along the x, y, and z axes. Photographs of the corresponding 3D architectures (A–H) are shown in Fig. 2. (b) Thermogravimetric analysis (TGA) data of the synthesized DEABMA polymer, showing weight loss (black curve), derivative weight (green curve), and heat flow (orange curve) as a function of temperature. (c) Fourier transform infrared (FTIR) spectra of samples heated to 500 °C under vacuum, followed by heat treatments at 900 °C, 1200 °C, and 1500 °C under a nitrogen atmosphere. (d) X-ray diffraction (XRD) patterns of samples treated at 500 °C under vacuum, followed by heat treatments at 900 °C, 1200 °C, and 1500 °C under a nitrogen atmosphere, compared with reference patterns from the Crystallography Open Database: h-BN (COD 96-101-0603) and B_2O_3 (COD 00-006-0297).

Compared to Fig. 1c, the FTIR spectrum recorded after initial heating to 500 °C exhibits a pronounced reduction in organic-related vibrational bands, indicating extensive polymer decomposition. Nevertheless, CH_2 stretching vibrations at 2965 cm^{-1}, 2840 cm^{-1}, and at 1390 cm^{-1}, attributed to C–N stretching, remain detectable with reduced intensity, suggesting incomplete removal of organic fragments at this stage. Concurrently, peaks at 1418 cm^{-1} and 1190 cm^{-1} emerge and are attributed to B–O and C–O related vibrations, indicating the initial formation of a boron, carbon, and oxygen-containing inorganic network. Further annealing at 900 °C and 1200 °C under nitrogen results in progressive spectral simplification, consistent with structural reorganization and formation of the inorganic phase. Weak absorption bands appearing after annealing at 1200 °C, particularly at 1373 cm^{-1} and 803 cm^{-1}, suggest the onset of B–N bond formation [22].

Following annealing at 1500 °C, the FTIR spectrum becomes nearly featureless, characteristic of a highly condensed and thermally stable inorganic material. This behavior is consistent with advanced ceramization and the formation of a predominantly BN-rich ceramic network. Overall, the FTIR results demonstrate a clear transformation from an organic polymer precursor to a fully inorganic, thermally stable ceramic structure as the annealing temperature increases from 500 °C to 1500 °C.

TGA and FTIR indicate that the majority of organic components are decomposed during thermal treatment, with residual carbonaceous species present at lower annealing temperatures (≤900 °C). With increasing temperature (≥1200 °C), the disappearance of C–H and C–N related bands suggests ceramization. However, the persistent black color of the structures indicates that carbon is not fully removed but remains in a transformed form, likely as amorphous carbon. Such residual carbon may partially block active sites or influence light absorption. This is consistent with the lower photocatalytic activity observed for samples treated at lower temperatures and the enhanced performance at higher temperatures, where BN formation becomes dominant.

X-ray diffraction (XRD) analysis was carried out to investigate the phase evolution of DEABMA-derived samples subjected to thermal treatment under different conditions. Fig. 4(c) presents the XRD diffractograms of samples annealed at 500 °C under vacuum, followed by annealing at 900 °C, 1200 °C, and 1500 °C in a nitrogen atmosphere. The phase evolution observed by XRD is in good agreement with the corresponding FTIR results, indicating a consistent transformation pathway upon increasing annealing temperature. The sample annealed at 500 °C under vacuum exhibits an XRD pattern dominated by boron oxide, with the most intensive diffraction at 27.74° (B_2O_3 COD 00-006-0297) [23]. This result is consistent with the FTIR spectra, which show intense B–O vibrational bands, indicating the formation of a boron–oxygen-rich phase after thermal treatment. Upon annealing at 900 °C in a nitrogen atmosphere, additional weak peaks appear, suggesting the formation of a secondary crystalline phase. At this stage, B_2O_3 remains the dominant component, while the emergence of the additional

phase indicates the onset of structural rearrangements and chemical transformations. Further increasing the annealing temperature to 1200 °C results in noticeable changes in the XRD pattern, indicating the formation of a polycrystalline structure. The diffractogram begins to exhibit characteristic peaks of hexagonal boron nitride (h-BN COD 96-101-0603) [24], indicating the onset of BN formation. Although the corresponding diffraction peaks remain low in intensity, their presence suggests the initial crystallization of BN within an inorganic matrix. This phase evolution is in good agreement with the FTIR spectra, in which the appearance of characteristic stretching and bending modes of B–N confirms the beginning of h-BN formation at this temperature. After annealing at 1500 °C in a nitrogen atmosphere, the XRD pattern is dominated by reflections characteristic of h-BN, with the most intense diffraction at 26.74°, overlapping with the broad amorphous background, which can be attributed to carbon. The diffraction peaks at the same positions as h-BN could also correspond to hexagonal graphite. However, FTIR confirms the presence of boron nitride, in excellent agreement with the FTIR analysis showing well-defined B–N vibrational bands and the absence of B–O, thereby confirming BN as the sole crystalline phase at the highest annealing temperature.

A carbothermal reduction mechanism commonly describes the formation of h-BN. However, a universally accepted reaction pathway for this transformation has not yet been established. Recent studies propose several possible mechanisms involving reactions between boron-containing precursors and nitrogen, with additional nitridation facilitated by nitrogen gas under high-temperature conditions [25–27]. In general, thermal treatment proceeds through several stages, including evaporation of volatile species, decomposition of the organic polymer network, and subsequent calcination, leading to the formation of boron–oxygen (B–O) and boron–carbon–oxygen (B–C–O) intermediates.

At elevated temperatures, these intermediates react with nitrogen gas in the presence of residual carbon to produce solid BN and gaseous CO. In this process, nitrogen gas plays a dual role, acting both as a chemical reactant and as a carrier gas that assists in the removal of CO from the reaction zone, thereby driving the reaction forward. From a thermodynamic perspective, the formation of BN becomes increasingly favorable at high temperatures due to its high stability and the continuous removal of gaseous reaction products, which shifts the equilibrium toward BN formation. However, the nitridation process is strongly kinetically limited and requires sufficiently high temperatures to overcome barriers associated with solid-state diffusion, bond rearrangement, and the removal of residual oxygen-containing species. The experimental results of the present study indicate that the transformation toward h-BN begins at approximately 1200 °C, with full conversion occurring at 1500 °C during pyrolysis. This relatively low onset temperature, compared to other systems, can be attributed to the presence of nitrogen within the precursor structure, which facilitates B–N bond formation and reduces diffusion limitations. In contrast, in systems lacking nitrogen in the initial precursor, BN formation is significantly delayed and typically initiates only at temperatures exceeding 1500–1700 °C [28], reflecting substantially higher kinetic barriers for nitrogen incorporation.

Overall, the FTIR and XRD results clearly demonstrate a temperature-driven phase transformation from polymeric to inorganic BN. The combined spectroscopic, diffraction, and thermal analyses consistently indicate that BN formation initiates at approximately 1200 °C and is completed after annealing at 1500 °C under a nitrogen atmosphere, reflecting a thermally activated, diffusion-limited nitridation process governed by both thermodynamic forces and precursor chemistry.

3.3. Investigation of the photocatalytic properties

The photocatalytic performance of the synthesized inorganic 3D structures was evaluated by monitoring the degradation of the organic dye Rhodamine B under halogen lamp irradiation, both in the presence and absence of the fabricated photocatalysts (PhCs). The temporal evolution of Rhodamine B absorption with irradiation time (0, 15, 30, 45, 60, 90 and 120 min), with and without PhCs in solution, together with the integrated absorption peak intensities, are presented in Appendix Figs: A.1, A.2, A.3, A.4, A.5. Photocatalytic activity was assessed for 3D structures with different architectures annealed at various temperatures, ranging from samples annealed at 500 °C under vacuum to those annealed at 900 °C, 1200 °C, and 1500 °C in a nitrogen atmosphere, structures depicted in Fig. 2. In the absorption spectra of solutions irradiated without PhCs, as well as those containing samples annealed at 500 °C and 900 °C, pronounced absorption bands remain even after 120 min of irradiation (Appendix Figs. A.1, A.2, and A.3), indicating the persistence of Rhodamine B in solution. In contrast, the presence of 3D structures annealed at 1200 °C and 1500 °C under a nitrogen atmosphere leads to a substantial reduction in absorption band intensity after 120 min for nearly all investigated architectures (Appendix Figs. A.4 and A.5), evidencing significant dye degradation. These results demonstrate that the fabricated PhCs exert a pronounced effect on the photocatalytic degradation of Rhodamine B.

The absorption band of Rhodamine B exhibits a pronounced shoulder, with the maximum located at 554 nm in the initial solution. After 120 min of photocatalytic treatment, this maximum shifts toward shorter wavelengths to approximately 548 nm. Owing to this spectral shift, the broad peak width, and the presence of a shoulder, the Lambert–Beer law cannot be applied reliably for direct concentration determination. Consequently, Rhodamine B degradation was quantified by integrating the absorption bands of the spectra (insets of Appendix Figs. A.1, A.2, A.3, A.4, and A.5). Using the integrated absorption intensities, the degradation efficiency of Rhodamine B (%) as a function of halogen lamp irradiation time was calculated for all investigated 3D-architectured photocatalyst architectures (A–H) annealed at 500 °C under vacuum and at 900 °C, 1200 °C, and 1500 °C under nitrogen. The resulting degradation efficiencies are summarized in Fig. 5.

In almost all cases of 3D architectured PhCs, a progressive increase in degradation efficiency is observed with increasing irradiation time up to 120 min. Only a few deviations are present, such as sample A annealed at 500 °C in N_2, where after 120 min the degradation efficiency is lower than that measured at shorter irradiation times. Such deviations may arise as a result of broadening or narrowing of the absorption band.

All architectures fabricated at 500 °C (Fig. 5a) exhibit relatively low photocatalytic activity, with degradation efficiencies remaining below 40% after 120 min of irradiation. Among the investigated geometries, architecture B stands out with the highest activity (70.71%). This may have been partly influenced by the fact that structure B annealed at 500 °C had the largest surface area (see Fig. 4(a)). Whereas the sample without a PhC structure demonstrates minimal degradation (13.61%), highlighting the beneficial role of the 3D architecture even after fabrication at low annealing temperatures. Annealing at 900 °C under N_2 (Fig. 5(b)) results in a reduction in photocatalytic performance for almost all PhC architectures (except A). After 120 min of irradiation, degradation efficiencies reach only 16.09–24.47%, depending on the geometry, which is only slightly higher than that of the sample without a PhC structure. This decrease can be attributed to the reduced surface area of structures annealed at higher temperatures; for example, the surface area of architecture B decreases from 6113 to 4173 mm^2 after annealing at 900 °C compared to annealing at 500 °C. In addition, no phase transformation into a more photocatalytically active material occurs during annealing at 900 °C in a nitrogen atmosphere. A pronounced increase in Rhodamine B degradation efficiency is observed for samples annealed at 1200 °C under N_2 (Fig. 5(c)) even with a decrease in active surface area. In this case, PhC architectures display significantly enhanced photocatalytic performance, with degradation efficiencies exceeding 80% for A, F, G architectures after 120 min of irradiation. Architecture F exhibits the highest activity, reaching

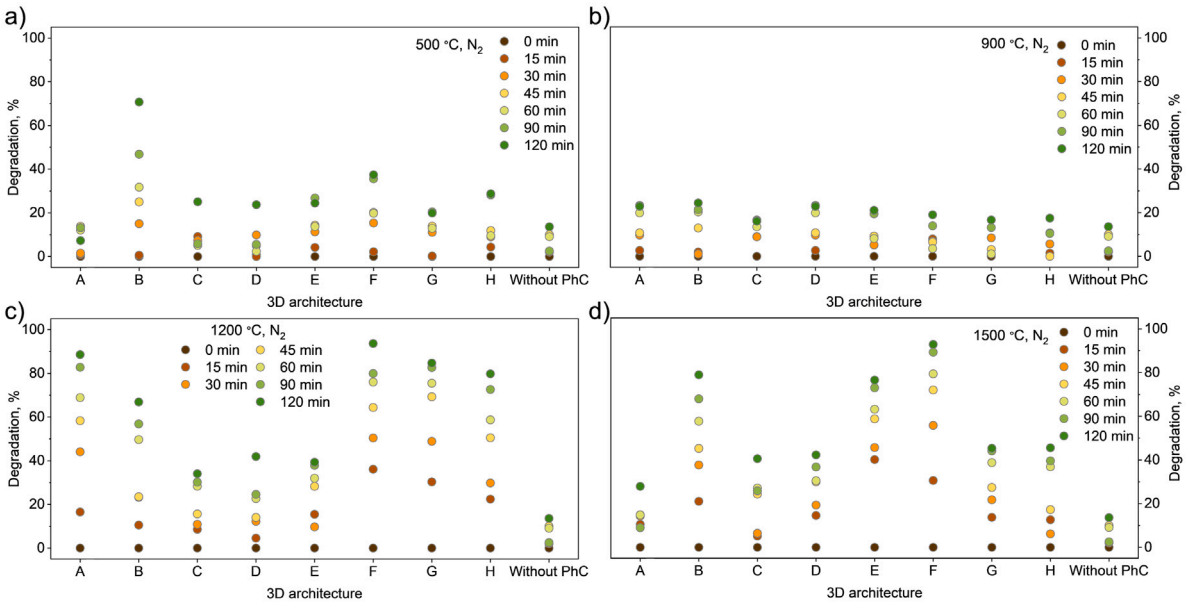

Fig. 5. Degradation efficiency (%) of Rhodamine B as a function of halogen lamp irradiation time (0–120 min) for different 3D architectured photocatalysts (PhCs) treated under the following conditions: (a) 500 °C under vacuum, (b) 900 °C under N_2, (c) 1200 °C under N_2, and (d) 1500 °C under N_2. Models and photographs of the corresponding 3D architectures (A–H) are shown in Fig. 2. The degradation efficiency of Rhodamine B increases markedly with both irradiation time and PhC annealing temperature. The highest degradation efficiencies were obtained for architecture F annealed at 1200 °C and 1500 °C under N_2, reaching 93.7% and 92.9% Rhodamine B degradation, respectively, after 120 min of irradiation, which represent the maximum values among all investigated PhC architectures and thermal treatment conditions.

93.67% degradation of Rhodamine B, closely followed by structures A (88.58%), G (84.67%), and H (79.79%). This confirms that, despite the reduced active surface area, the enhanced photocatalytic efficiency is governed by a favorable material transformation at this temperature, as evidenced by XRD and FTIR data indicating the onset of h-BN formation. Using PhCs fabricated at 1500 °C (Fig. 5d), high photocatalytic activity is retained across most PhC architectures, with maximum degradation efficiencies comparable to those obtained at 1200 °C. Architecture F again demonstrates the highest performance, achieving 92.90% Rhodamine B degradation after 120 min. The reusability of the photocatalyst was evaluated using the same F-architecture PhC annealed at 1200 °C over three consecutive RhB degradation cycles under identical conditions (see Appendix Fig. A.8). Despite a gradual decrease in degradation efficiency (92.90%, 69.35%, and 55.25% for the first, second, and third cycles), the catalyst retained significant photocatalytic activity over a total of 360 min, demonstrating its operational stability and durability. Variations of degradation efficiencies between architectures are observed without any correlation in Fig. 5, indicating that while thermal treatment strongly enhances activity, the specific geometry and surface area continues to influence photocatalytic efficiency.

Therefore, the influence of the 3D structural geometry and material nature on the photocatalytic activity was evaluated. To this end, the specific degradation efficiencies, expressed as the mass of Rhodamine B degraded per unit surface area of the PhC (mg/m^2), were calculated as a function of halogen lamp irradiation time (0–120 min) for different 3D architectured PhCs. The specific degradation efficiencies were calculated for the same PhCs (A–H) annealed at 500 °C under vacuum, 900 °C under N_2, 1200 °C under N_2, and 1500 °C under N_2. The results are presented in Fig. 6.

The degradation efficiency is expressed as the mass of the dye degraded per unit of surface area (mg/m^2), allowing for a direct comparison between architectures with different geometrical characteristics. As a result, Fig. 6 shows much clearer trends than Fig. 5. After annealing at 500 °C under vacuum (Fig. 6(a)), all architectures exhibit low specific photocatalytic activity. With increasing irradiation time, only a slight increase in degradation efficiency is observed, and the maximum value remains low, reaching 76.10 mg/m^2 for the H structure even after 120 min of exposure. Annealing at 900 °C (see Fig. 6(b)) also did not produce favorable results. After 120 min of exposure, the highest specific photocatalytic activity was observed for the H structure, reaching only 65.50 mg/m^2. This indicates that annealing to 900 °C is insufficient to convert the material into a photocatalytically active phase. Therefore, architectural differences cannot be reliably evaluated under these conditions.

Annealing at 1200 °C under an atmosphere of N_2 (Fig. 6(c)) leads to a pronounced enhancement in the specific photocatalytic efficiency across all architectures. The degradation efficiency increases with irradiation time, and a clearer differentiation between the various 3D models becomes evident. Architectures F–H exhibit higher specific degradation efficiency than structures A–E. This indicates that more complex architectures, such as curved shapes (G and H) or mesh-type gyroid (F), are more effective than channel (A), lattice (E), diamond-type (B), and conventional gyroid geometries (C and D). Architecture H exhibits the highest activity, reaching a maximum specific degradation efficiency of 355.01 mg/m^2 after 120 min of irradiation. This substantial enhancement demonstrates that annealing at 1200 °C strongly promotes the formation of a photocatalytically active material.

Further annealing of the 3D structures at 1500 °C under N_2 and their subsequent use in photocatalytic degradation experiments preserve high photocatalytic activity across all advanced architectures (Fig. 6(d)), although the maximum efficiencies are slightly reduced compared with those of structures annealed at 1200 °C. Architecture H exhibits the highest performance, reaching 259.29 mg/m^2 after 120 min, while architectures E–G show markedly enhanced degradation efficiencies relative to architectures A–D. Although FTIR and XRD data confirmed the formation of the h-BN phase after annealing at 1500 °C. The observed photocatalytic activity under visible light cannot be attributed to pristine h-BN (band gap ≈5.95 eV [29]), but rather to the formation of a carbon-modified BN-based material during pyrolysis. Amorphous carbon (band gap 1.5–2.3 eV [30]) and its incorporation into the BN lattice through C–B and C–N bond formation reduce the effective band gap to ≈2.0 eV [31], enabling visible-light absorption

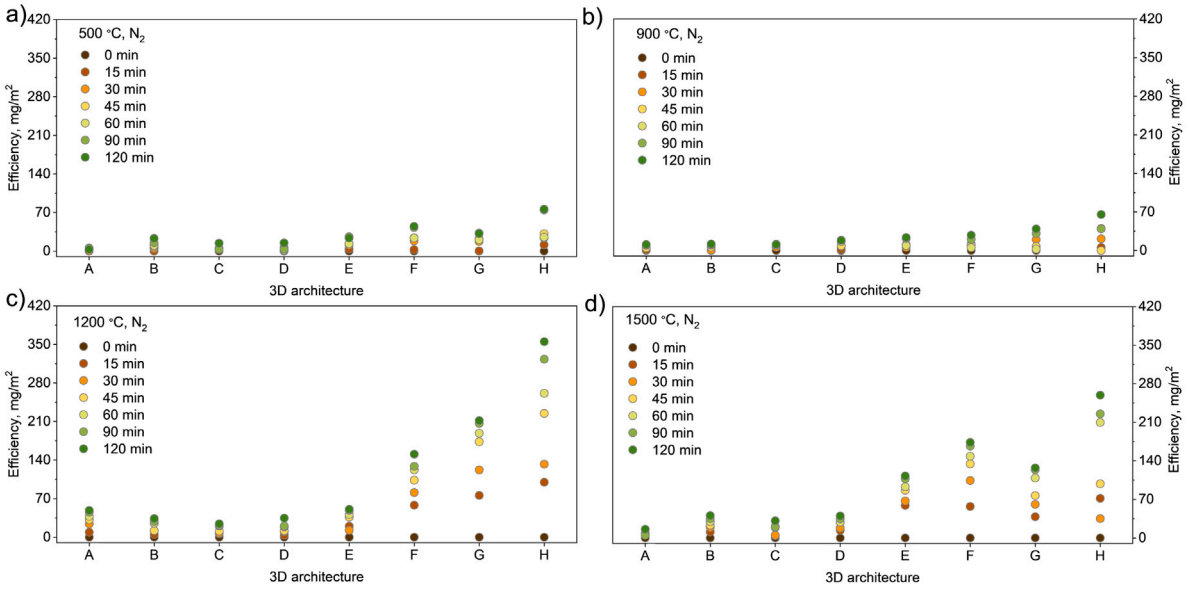

Fig. 6. Specific degradation efficiencies of Rhodamine B, expressed as the mass degraded per unit surface area of the photocatalyst (mg/m^2), as a function of halogen lamp irradiation time (0–120 min) for different 3D architectured PhCs treated under the following conditions: (a) 500 °C under vacuum, (b) 900 °C under N_2, (c) 1200 °C under N_2, and (d) 1500 °C under N_2. Models and photographs of the corresponding 3D architectures (A–H) are shown in Fig. 2. The highest specific degradation efficiency is achieved for the 3D architectured PhC H annealed at 1200 °C and 1500 °C under N_2, reaching values of 355.01 mg/m^2 (1200 °C) and 259.29 mg/m^2 (1500 °C) after 120 min of irradiation, indicating that both: material composition achieved by high temperature annealing and optimized 3D architecture are key factors governing maximum photocatalytic performance.

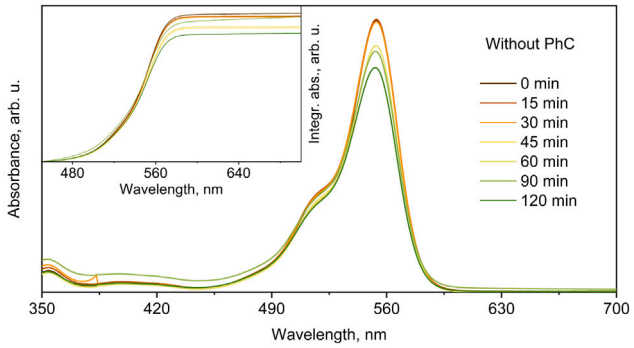

Fig. A.1. Time-dependent changes in the UV–Vis absorption spectra of Rhodamine B solution under halogen lamp irradiation in the absence of 3D objects.

under halogen lamp irradiation. This lattice-level electronic modification increases charge carrier density (≈2.97 × 10^{19} cm^{-3} [31]), enhances electron delocalization, and improves charge separation and transport, resulting in significantly enhanced photocatalytic performance. However, structures annealed at 1500 °C, did not exhibit the highest specific degradation efficiency. This is likely because partial structural deformation occurred at this temperature. The H architecture annealed at 1500 °C could have been more efficient if deformation had not taken place, since the specific efficiency was calculated using the theoretical surface area. Due to partial melting-induced deformation, some structural cavities became partially closed, resulting in a reduced actual surface area and decreased permeability of the Rhodamine B solution. These effects likely contributed to the lower specific degradation efficiency compared to structures annealed at 1200 °C.

However, geometric surface area alone does not fully reflect photocatalytic performance, as pyrolysis temperature critically determines phase composition, defect structure, and electronic properties. In this study, annealing (≥1200 °C) induces transformation to BN and significantly enhances activity despite surface area reduction, indicating that intrinsic performance is governed by phase and defect states. Additionally, light distribution, mass transport, and 3D architecture further influence the effective utilization of active sites. To elucidate the underlying relationships and mechanisms more precisely, PhCs annealed at intermediate temperatures between 1200 °C and 1500 °C should be systematically investigated.

The Langmuir–Hinshelwood model [28,32] was used to describe the relationship between the photocatalytic decolorization rate of Rhodamine B in the presence of 3D PhCs as a function of the irradiation time. The rate equation is expressed as follows:

$$\frac{-dC}{dt} = \frac{k_{L-H} K_{ad} C}{1 + K_{ad} C} \tag{1}$$

where K_{ad} is the reactant adsorption coefficient on the PhC surface, k_{L-H} is the Langmuir–Hinshelwood reaction rate constant, and C is the concentration of Rhodamine B at time t. The values of k_{L-H} and K_{ad} are used to evaluate the influence of light intensity on the equilibrium constant that governs the rapid adsorption–desorption processes between the surface monolayer on PhC and the bulk solution. By integrating Eq. (1), the following expression is obtained:

$$\ln\left(\frac{C_0}{C}\right) = K_{ad}(C - C_0) + k_{L-H} K_{ad} t \tag{2}$$

where C_0 is the initial concentration of Rhodamine B. For a pseudo-first-order reaction, the term $K_{ad}C$ is minimal compared to unity in the denominator of Eq. (1), allowing the expression of the rate to be simplified. Upon integration, the following linearized form is obtained:

$$\ln\left(\frac{C_0}{C}\right) = k_{L-H} K_{ad} t = kt \tag{3}$$

where $k = k_{L-H} K_{ad}$ is the pseudo-first-order reaction rate constant.

A linear relationship was observed between the natural logarithm of the Rhodamine B concentration ratio ($\ln(C_0/C)$) and the corresponding irradiation time, as shown in Appendix Fig. A.6. This indicates that the photocatalytic degradation of Rhodamine B follows pseudo-first-order reaction kinetics. It is important to note that the dependence of the natural logarithm of the Rhodamine B concentration ratio on

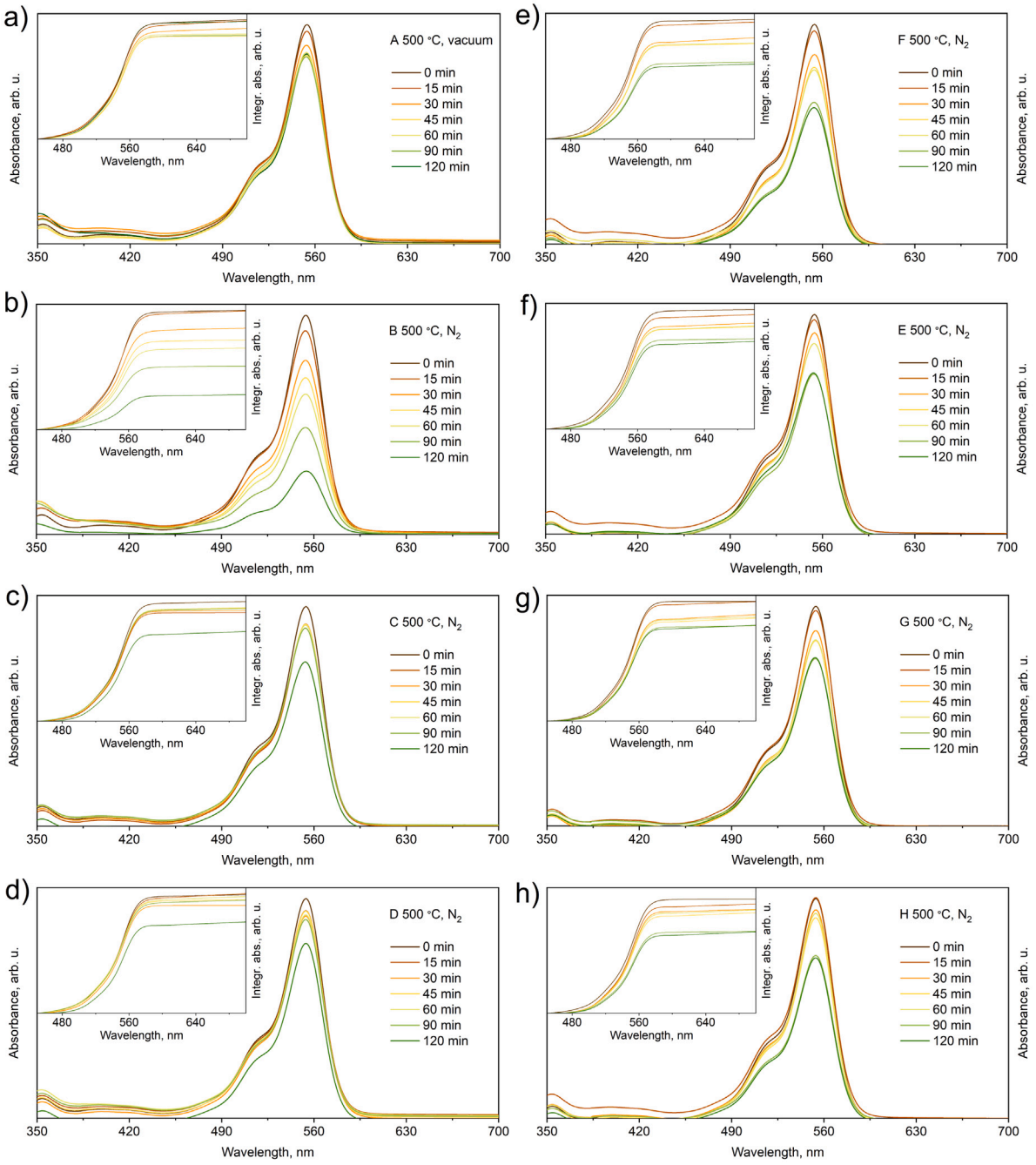

Fig. A.2. Time-dependent UV–Vis absorption spectra of Rhodamine B solutions under halogen lamp irradiation in the presence of 3D objects with different shapes and surface areas (A–H, corresponding to (a)–(h)), fabricated by UV stereolithography and treated at 500 °C under vacuum. Photographs of corresponding 3D architectures (A–H) are shown in Fig. 2.

time did not exhibit a linear relationship for all samples. Specifically, samples A, C, and D annealed at 500 °C under vacuum; samples C, F, G, and H annealed at 900 °C under N_2; and sample A annealed at 1500 °C exhibited linear fits with R^2 values below 0.94. Therefore, the calculated reaction rate constants for these samples are not reliable, as they should be determined using a different reaction order model. For the samples that exhibited a linear relationship, the absolute values of the rate constants, independent of the active surface area or mass of the 3D structures, are presented in Fig. A.7. The results indicate that the highest photocatalytic degradation rate was achieved for the PhC F architecture annealed at 1500 °C ($k = 0.0241 \pm 0.0009$ min^{-1}), followed by the F architecture annealed at 1200 °C ($k = 0.0217 \pm 0.0010$ min^{-1}). In contrast, for the H architecture annealed at 1200 °C, which exhibited the highest degradation efficiency, the determined degradation rate constant was $k = 0.0139 \pm 0.0003$ min^{-1}.

Overall, these results reveal a strong synergistic effect between material nature and 3D architectural shape. High-temperature treatment (more than 1200 °C) is essential for achieving high intrinsic photocatalytic activity, whereas optimized 3D architectures, particularly

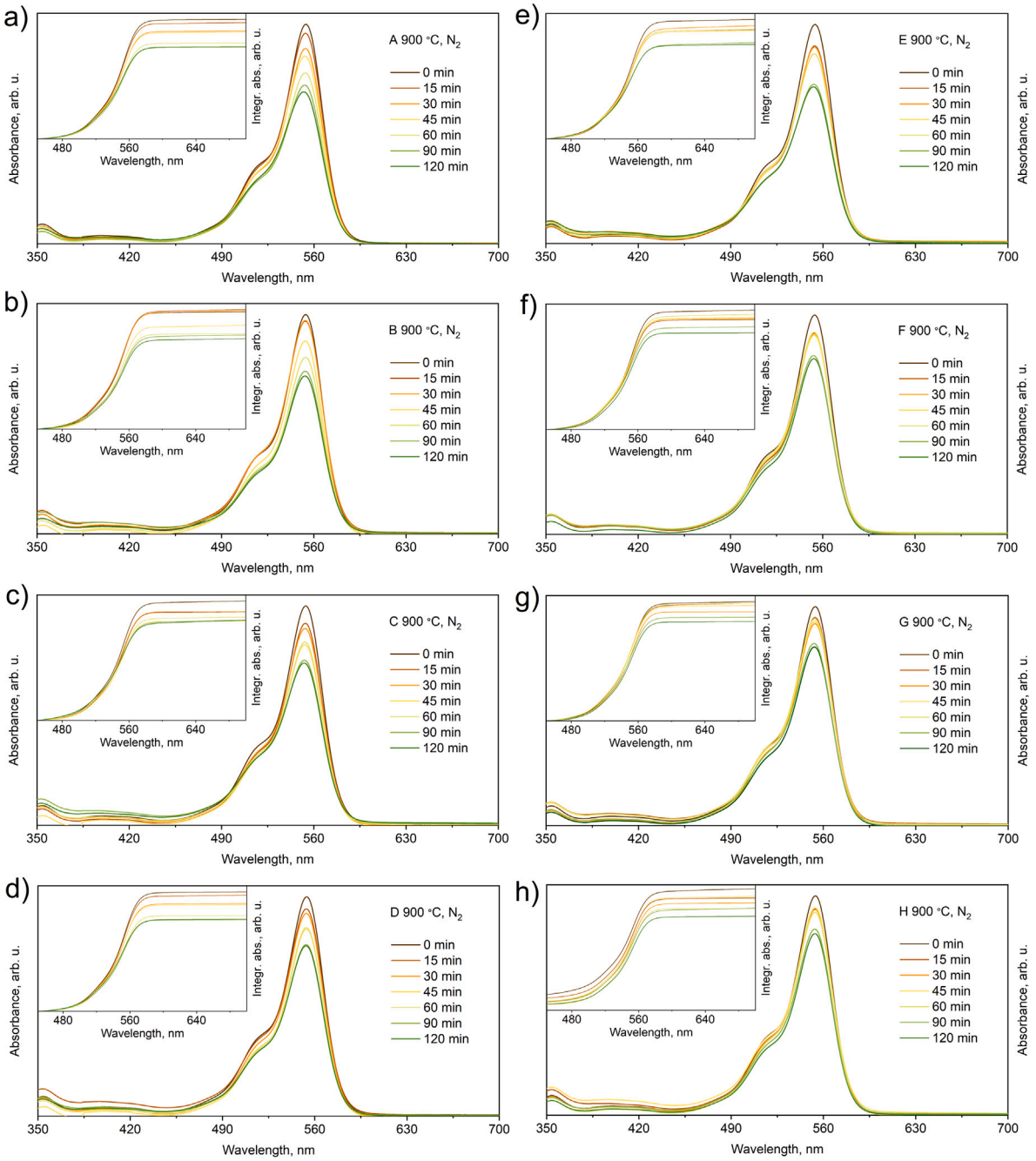

Fig. A.3. Time-dependent UV–Vis absorption spectra of Rhodamine B solutions under halogen lamp irradiation in the presence of 3D objects with different shapes and surface areas (A–H, corresponding to (a)–(h)), fabricated by UV stereolithography and treated at 500 °C under vacuum, and subsequently annealed at 900 °C under N_2 atmosphere. Photographs of corresponding 3D architectures (A–H) are shown in Fig. 2.

architecture H, are crucial for maximizing the specific degradation efficiency, confirming that both material processing and structural model are key parameters controlling photocatalytic performance.

4. Conclusions

This study demonstrates a polymer-derived ceramic route for fabricating monolithic 3D photo-catalysts by combining the synthesis of a novel boron and nitrogen-containing acrylate with UV stereolithography and high-temperature pyrolysis. Controlled thermal conversion enabled the transformation of printed polymer scaffolds into mechanically stable boron-based ceramics, with the onset of BN formation at 1200 °C and the predominant crystallization of h-BN after annealing at 1500 °C.

Photocatalytic degradation of Rhodamine B revealed that performance is governed not only by the composition of the material but also by the 3D architecture. Structures treated at 500 °C and 900 °C exhibited limited photocatalytic activity, whereas annealing at 1200 °C resulted in a pronounced increase in photocatalytic efficiency despite surface-area reduction due to shrinkage and densification. When the

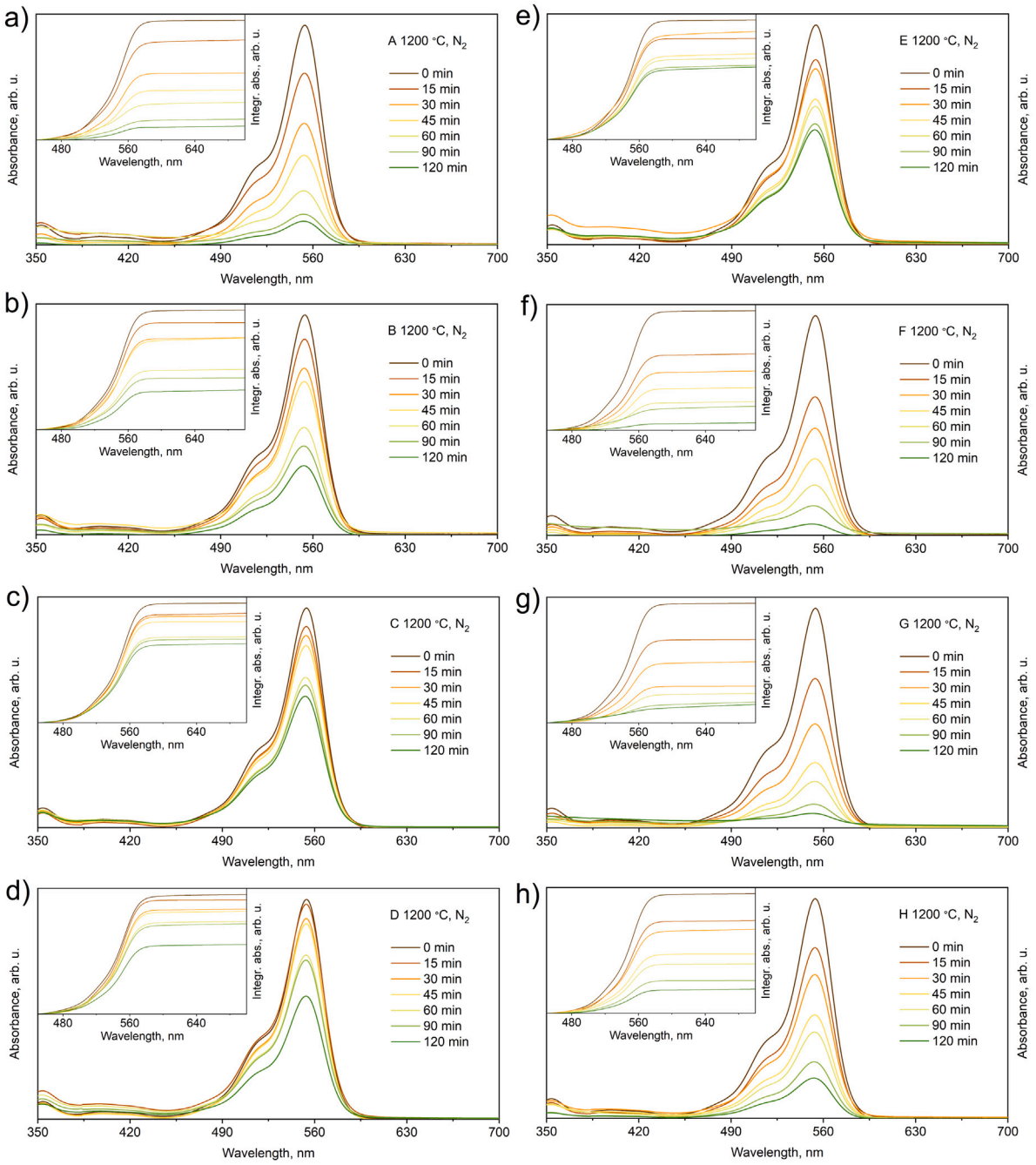

Fig. A.4. Time-dependent UV–Vis absorption spectra of Rhodamine B solutions under halogen lamp irradiation in the presence of 3D objects with different shapes and surface areas (A–H, corresponding to (a)–(h)), fabricated by UV stereolithography and treated at 500 °C under vacuum, and subsequently annealed at 1200 °C under N_2 atmosphere. Photographs of corresponding 3D architectures (A–H) are shown in Fig. 2.

degradation efficiency was expressed as the mass degraded per unit surface area of the PhC, rounded gyroid-type architectures significantly outperformed channel and lattice-based models, underscoring the role of architecture in light penetration and mass transport. The highest specific degradation efficiency of 355.01 mg/m^2 was achieved for the gyroid-based rounded architecture (H) annealed at 1200 °C. At the same time, a lower value was observed at 1500 °C (259.29 mg/m^2) due to partial structural deformation. To the best of our knowledge, such rounded geometries based on gyroids have not previously been explored in photocatalytic systems and demonstrate superior performance through enhanced light–material interaction and mass transport.

Overall, these findings underscore a strong interdependence between material chemistry and architectural model, demonstrating that optimal photocatalytic performance arises not solely from phase composition but also from geometry-driven enhancement of light–material interactions. This work establishes three-dimensional architected

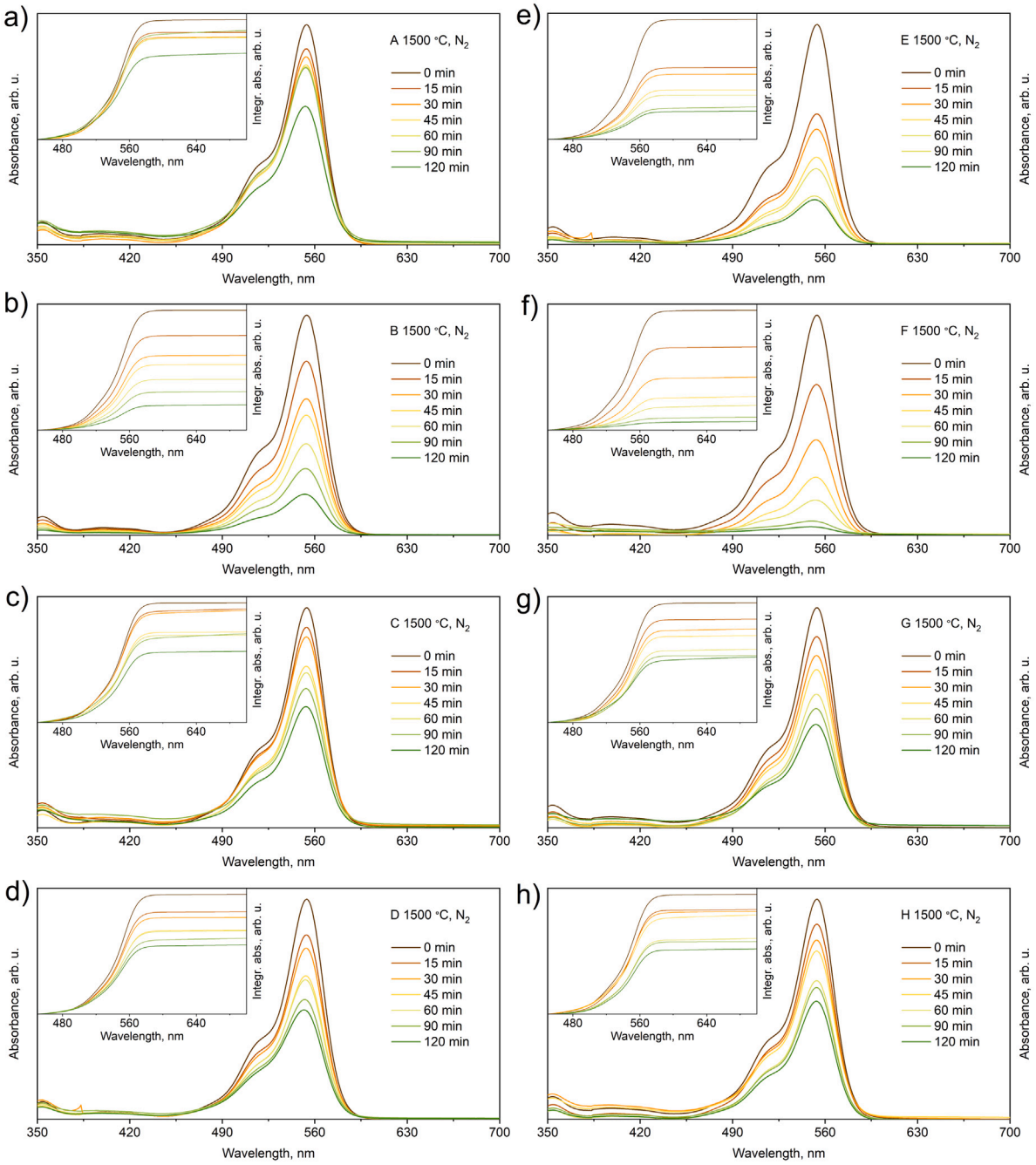

Fig. A.5. Time-dependent UV–Vis absorption spectra of Rhodamine B solutions under halogen lamp irradiation in the presence of 3D objects with different shapes and surface areas (A–H, corresponding to (a)–(h)), fabricated by UV stereolithography and treated at 500 °C under vacuum, and subsequently annealed at 1500 °C under N_2 atmosphere. Photographs of corresponding 3D architectures (A–H) are shown in Fig. 2.

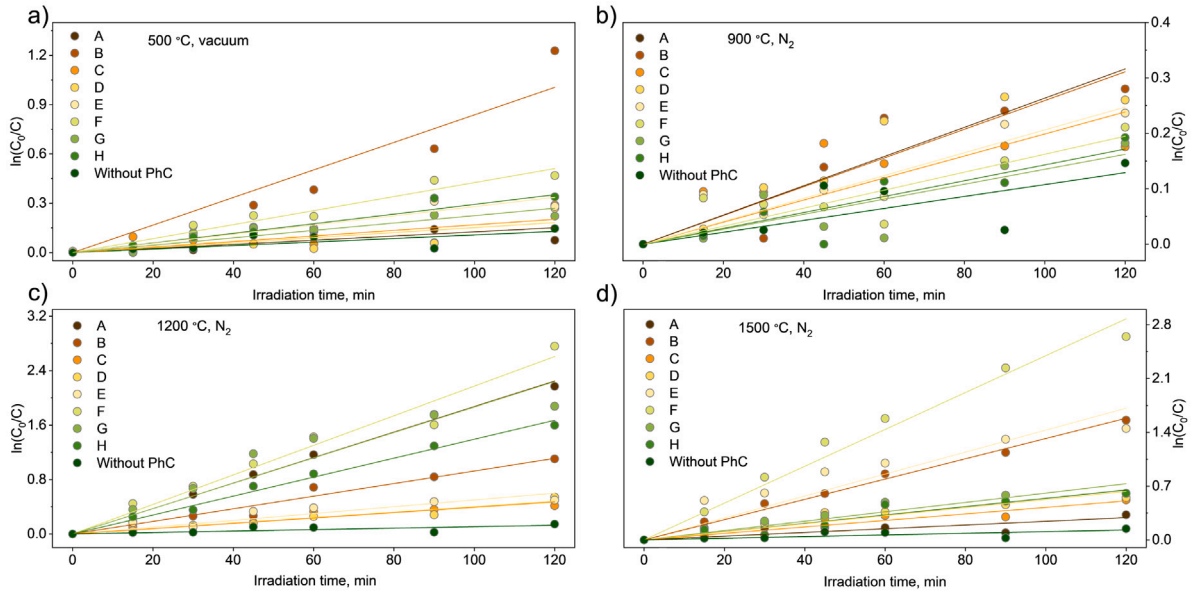

Fig. A.6. The logarithm of the ratio between the original concentration of Rhodamine B and the concentration after photocatalytic degradation under halogen lamp irradiation with PhC and without ($\ln(C_0/C)$) versus the corresponding irradiation duration (min) for different 3D architectured photocatalysts (PhCs) treated under the following conditions: (a) 500 °C under vacuum, (b) 900 °C under N_2, (c) 1200 °C under N_2, and (d) 1500 °C under N_2. Models and photographs of the corresponding 3D architectures (A–H) are shown in Fig. 2.

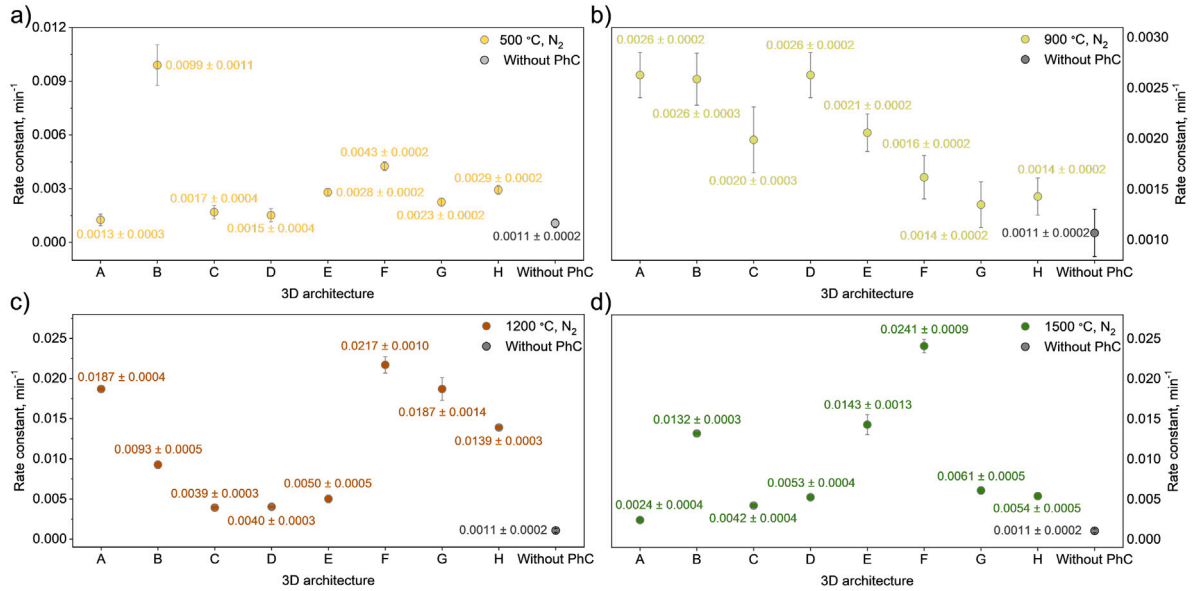

Fig. A.7. Degradation rate constants of Rhodamine B as a function of photonic crystal (PhC) architecture for various 3D-architectured photocatalysts subjected to different thermal treatment conditions: (a) 500 °C under vacuum, (b) 900 °C under N_2, (c) 1200 °C under N_2, and (d) 1500 °C under N_2. The corresponding models and photographs of the 3D architectures (A–H) are presented in Fig. 2.

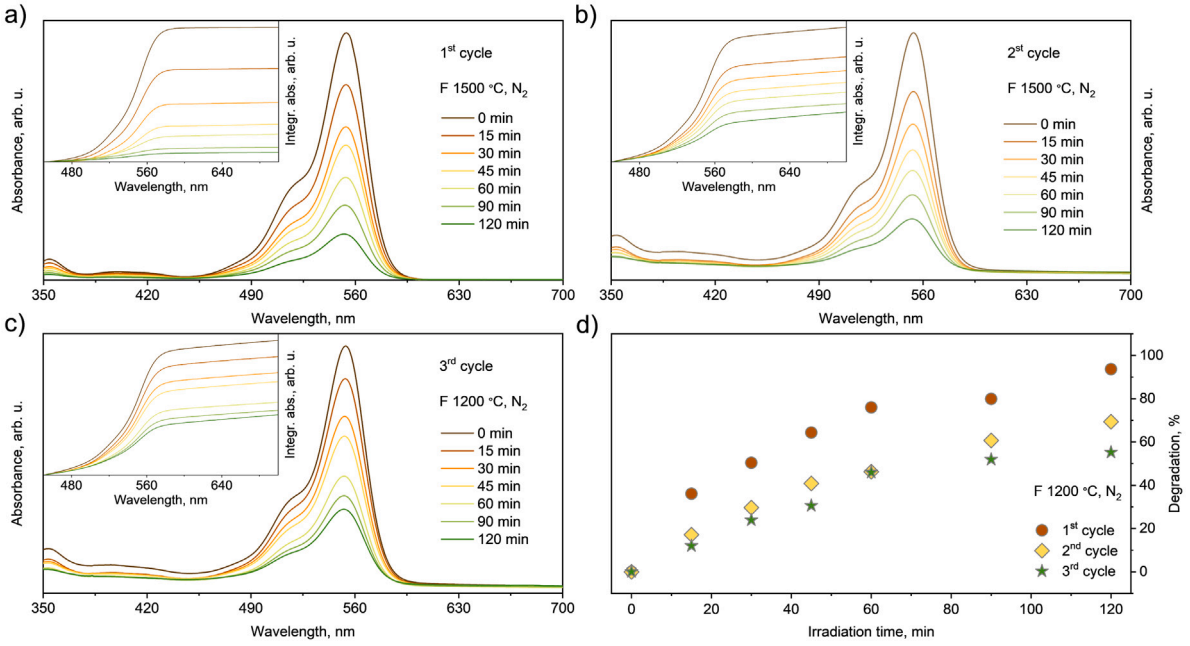

Fig. A.8. Reusability evaluation of F architecture, annealed at 1200 °C under N_2 during RhB photocatalytic degradation. (a–c) UV–VIS absorption spectra of RhB during three consecutive degradation cycles: (a) first cycle, (b) second cycle, and (c) third cycle. (d) Comparison of degradation efficiencies as a function of irradiation time for the three cycles, showing the final degradation efficiency after 120 min (92.90%, 69.35%, and 55.25% for the first, second, and third cycles, respectively), demonstrating that the photocatalyst retains its activity even after 360 min of operation.

polymer-derived ceramics as a robust, reusable, and scalable platform for sustainable photocatalytic water-treatment technologies.

CRediT authorship contribution statement

Greta Merkininkaitė: Writing – original draft, Visualization, Supervision, Methodology, Investigation, Funding acquisition, Formal analysis, Data curation, Conceptualization. **Robertas Virkėtis:** Investigation, Formal analysis. **Simas Šakirzanovas:** Writing – review & editing, Supervision, Resources.

Declaration of competing interest

The authors declare the following financial interests/personal relationships which may be considered as potential competing interests: Greta Merkininkaite reports financial support was provided by Research Council of Lithuania (LMTLT) Fund. If there are other authors, they declare that they have no known competing financial interests or personal relationships that could have appeared to influence the work reported in this paper.

Acknowledgment

This work was supported by the Research Council of Lithuania (LMTLT) Fund [grant number S-PD-24-40].

Appendix

See Figs. A.1–A.8.

References

[1] T. Bekele, G. Alamnie, The photocatalytic degradation of organic pollutants-a comprehensive overview, Results Chem. 18 (2025) 102758.

[2] Y. Wang, Y. Zhang, S. Wang, Y. Guan, Y. Zhang, A 3D printed synergistic aerogel microreactor toward stable and high-efficiency photocatalytic degradation, Mater. Today Chem. 22 (2021) 100566.

[3] A.O. Yusuf, S.A. Jitan, R. Al Sakkaf, H.S. Jarusheh, C. Garlisi, L.F. Dumée, G. Palmisano, 3D printing to enable photocatalytic process engineering: A critical assessment and perspective, Appl. Mater. Today 35 (2023) 101940.

[4] C. Xu, T. Liu, W. Wei, Y. Sun, C. Liang, K. Cao, T. Guan, Z. Liang, L. Jiang, 3D printing of powder-based inks into functional hierarchical porous TiO_2 materials, Adv. Eng. Mater. 22 (3) (2020) 1901088, arXiv:https://advanced.onlinelibrary.wiley.com/doi/pdf/10.1002/adem.201901088.

[5] S. wei Bai, H. Mei, M. gang Zhang, S. xiang Zhou, Y. kai Yan, L. fei Cheng, L. tong Zhang, J. Lu, 3D printing assemble technology toward advanced photocatalysis, Mater. Today Nano 24 (2023) 100385.

[6] I.S.O. Barbosa, Y.A. Manrique, D. Paiva, J.L. Faria, R.J. Santos, C.G. Silva, Efficient photocatalytic reactors via 3D printing: SLA fabrication and TiO_2 hybrid materials, RSC Adv. 15 (4) (2025) 2275–2286.

[7] D.-S. Cheon, M. Takahashi, T. Kim, Permeability differences based on three-dimensional geometrical information of void spaces, J. Rock Mech. Geotech. Eng. 13 (2) (2021) 368–376.

[8] L. Pan, M. Zhang, H. Mei, L. Yao, Z. Jin, H. Liu, S. Zhou, Z. Yao, G. Zhu, L. Cheng, L. Zhang, 3D bionic reactor optimizes photon and mass transfer by expanding reaction space to enhance photocatalytic CO_2 reduction, Sep. Purif. Technol. 301 (2022) 121974.

[9] B. Kaur, P. Singh, S. Thakur, A. Singh, V. Chaudhary, N. Kumar, A.A.P. Khan, M.A. Rub, N. Azum, P. Raizada, Harnessing 3D printing for tailored TiO_2 structures redefining organic pollutant degradation, J. Env. Chem. Eng. 13 (2) (2025) 116042.

[10] N. Li, K. Tong, L. Yang, X. Du, Review of 3D printing in photocatalytic substrates and catalysts, Mater. Today Energ. 29 (2022) 101100.

[11] Y. Majooni, S.P. Sava, K. Fayazbakhsh, N. Yousefi, Sustainable 3D-printed platforms with durable photocatalytic coatings for efficient water treatment, Adv. Sustain. Syst. 9 (8) (2025) e00135.

[12] C. Akarsu Dülgar, T. Çakır Çanak, E. Serhatli, Effect of boron acrylate monomer content and multi-acrylate functional boron methacrylate on adhesive performance for water-borne acrylic polymers, Polym. Bull. 76 (2019) 1–19.

[13] R. Peamsuwan, P. Waramit, I. Worapun, B. Krittacom, T. Phoo-Ngernkham, R. Luampon, Investigation of tungsten halogen lamp for possible usage as heat source for testing solar collector, Energy Built Env. 5 (4) (2024) 517–528.

[14] Radium Lampenwerk GmbH, 2026, [Online]. Available: https://www.radium.de/en (Accessed 22 April 2026).

[15] A. Hoffmann, K. Kreuels, A. Gillner, Novel thiol-ene photo resins for stereolithography with enhanced mechanical and optical properties, Macromol. Mater. Eng. 307 (4) (2022) 2100625.

[16] G. Feigl, D. Zaugg, J. Hinum-Wagner, S. Hörmann, A. Bergmann, Refractive index characterization and modeling of polymerization-dependent refractive index variations in two-photon polymerization resins, Opt. Contin. 4 (2025) 996–1005.

[17] F. Aloui, L. Lecamp, P. Lebaudy, F. Burel, Refractive index evolution of various commercial acrylic resins during photopolymerization, Express Polym. Lett. 12 (2018) 966–971.
[18] A. Ribas-Massonis, M. Cicujano, E. Besalú, A. Poater, Free-radical photopolymerization for curing products for refinish coatings market, Polymers 14 (2022) 2856.
[19] Proactively seeking viscosity correction, 2018, [Online]. Available: https://www.pumpsandsystems.com/proactively-seeking-viscosity-correction, (Accessed 23 January 2026).
[20] A. Chakraborty, Samriti, O. Ruzimuradov, R.K. Gupta, J. Cho, J. Prakash, TiO_2 nanoflower photocatalysts: Synthesis, modifications and applications in wastewater treatment for removal of emerging organic pollutants, Environ. Res. 212 (2022) 113550.
[21] S. Wang, Y. Wang, C. Bian, Y. Zhong, X. Jing, The thermal stability and pyrolysis mechanism of boron-containing phenolic resins: The effect of phenyl borates on the char formation, Appl. Surf. Sci. 331 (2015) 519–529.
[22] H. Zhang, B.-G. Shin, D.-e. Lee, K.-B. Yoon, Preparation of PP/2D-Nanosheet composites using $MoS_2/MgCl_2$- and $BN/MgCl_2$-Bisupported Ziegler–Natta catalysts, Catalysts 10 (2020) 596.
[23] X. Zhao, Q. Zhang, B. Zhang, C.-M. Chen, J. Xu, A. Wang, D. Su, T. Zhang, Decorated resol derived mesoporous carbon: Highly ordered microstructure, rich boron incorporation, and excellent electrochemical capacitance, RSC Adv. 3 (2013) 3578–3584.
[24] A. Brager, An X-Ray examination of the structure of boron nitride, Cta Phys.-Chim. Sin. 7 (1937) 699–706.
[25] A. Aydoğdu, N. Sevinç, Carbothermic formation of boron nitride, J. Eur. Ceram. Soc. 23 (16) (2003) 3153–3161.
[26] C.S. Chari, B.W. McEnerney, R.R. Hofer, J.A. Wollmershauser, E.P. Gorzkowski, K.T. Faber, High-temperature carbothermal synthesis and characterization of graphite/h-BN bimaterials, J. Am. Ceram. Soc. 106 (4) (2023) 2225–2239.
[27] Y.M.Z. Ahmed, S.M. El-Sheikh, A.A.-E.-B. Abd Allah, S. Anwar, Thermal properties and formation mechanism of h-BN nanoneedles synthesized via carbothermic reduction reaction, Int. J. Appl. Ceram. Technol. 15 (1) (2018) 42–52.
[28] R. Virkėtis, V. Klimkevičius, T. Murauskas, S. Šakirzanovas, L. Vilčiauskas, G. Merkininkaitė, Self-supporting 3D boron-based photocatalyst prototype for water treatment, Adv. Eng. Mat. n/a (n/a) (2026) e202503003.
[29] M. Legesse, S.N. Rashkeev, H. Saidaoui, F.E. Mellouhi, S. Ahzi, F.H. Alharbi, Band gap tuning in aluminum doped two-dimensional hexagonal boron nitride, Mater. Chem. Phys. 250 (2020) 123176.
[30] G.D. Gesesse, A. Gomis-Berenguer, M.-F. Barthe, C.O. Ania, On the analysis of diffuse reflectance measurements to estimate the optical properties of amorphous porous carbons and semiconductor/carbon catalysts, J. Photochem. Photobiol. A: Chem. 398 (2020) 112622.
[31] N.S. Mishra, P. Saravanan, LED-light-activated photocatalytic performance of metal-free carbon-modified hexagonal boron nitride towards degradation of methylene blue and phenol, Beilstein J. Nanotechnol. 13 (2022) 1380–1392.
[32] M. Mahmoud, A. Poncheri, Y. Badr, M. Wahed, Photocatalytic degradation of methyl red dye, South Afr. J. Sci. 105 (2009) 299–303.